# Observation of the experimental propagation properties of Helmholtz-Gauss beams

**Carlos López-Mariscal,** MEMBER SPIE
**Miguel A. Bandres,** MEMBER SPIE
**Julio C. Gutiérrez-Vega,** MEMBER SPIE
Tecnológico de Monterrey
Photonics and Mathematical Optics Group
Monterrey, México 64849

**Abstract.** We present the experimental generation and characterization of each one of the four fundamental families of Helmholtz-Gauss beams: cosine-Gauss beams, stationary and helical Mathieu-Gauss beams, stationary and traveling parabolic-Gauss beams, and Bessel-Gauss beams. Both the transverse intensity profile and power spectrum that each one of the beams exhibits upon propagation is observed and compared to the theoretical model with good quantitative agreement. Emphasis is made on the fact that each of the four families of HzG beams is complete and orthogonal, and thus of fundamental relevance.  [DOI: 10.1117/1.2210485]

Subject terms: paraxial wave equations; nondiffracting beams; holographic methods; Bessel-Gauss beams.

Paper 050680R received Aug. 18, 2005; revised manuscript received Nov. 8, 2005; accepted for publication Nov. 25, 2005; published online Jun. 7, 2006.

## 1 Introduction

Nondiffracting optical beams are known to propagate indefinitely without change of their transverse shape under ideal conditions.[1] Given the separability properties of Helmholtz equation (HE), there exist four fundamental families of ideal nondiffracting optical beams, each one associated to a corresponding coordinate system. Namely, plane waves, Bessel beams,[2,3] Mathieu beams,[4–6] and parabolic beams[7] for Cartesian, circular cylindrical, elliptic cylindrical, and parabolic cylindrical coordinates, respectively. In this context, the term 'fundamental' refers to a family of ideal nondiffracting beams which are eigenmodes of the Helmholtz equation in a cylindrical orthogonal coordinate system. A fundamental family constitutes a basis of eigenfunctions for expanding any nondiffracting beam with the same transverse spatial frequency.

A Helmholtz-Gauss (HzG) beam is in turn the wavefield described at the plane $z=0$ by the product of a solution of the two-dimensional Helmholtz equation (i.e., the transverse field of an arbitrary nondiffracting beam) and a radial Gaussian function. In particular, Bessel-Gauss (BG) beams are a special case of HzG beams.[8,9] Gutiérrez-Vega and Bandrés[10] recently reported a closed-form expression for the paraxial propagation and the angular spectrum of the HzG beams and provided explicit expressions for each one of the fundamental families: cosine-Gauss (CG) beams in Cartesian coordinates, Mathieu-Gauss (MG) beams in elliptic coordinates, and parabolic-Gauss (PG) beams in parabolic coordinates. In contrast to ideal nondiffracting beams, HzG beams carry finite power and can be experimentally generated to a close approximation to their ideal functional form.

We report in the present work the experimental generation and characterization of each fundamental family of HzG beams. We describe the field distribution that characterizes every family and we characterize their transverse intensity distribution experimentally and their evolution upon propagation. We also observe the power spectra of these beams and record their spatial intensity variation and compare our observations with theoretical predictions.[10]

A feature of special interest is that of MG and PG beams on free-space propagation. In particular, we observe a twisting behavior that the transverse energy flow presents with specific spatial characteristics inherent to the spatial properties of the wavefields.[11,12] Since each family of HzG beams forms a basis for expanding any HzG beam, their study is of fundamental importance. Potential applications of HzG beams include manipulation of microparticles,[13] metrology, microlithography,[14] medical imaging,[15] nonlinear optics and optical and wireless communications among others.[16]

## 2 Definition of Helmholtz-Gauss Beams

We briefly describe HzG beams in order to establish notation and to provide a reference point for necessary formulas. Suppose that a monochromatic wave $U(\mathbf{r})$ with time dependence $\exp(-i\omega t)$ has a disturbance across the plane $z=0$ given by

$$U_0(\mathbf{r}_t) = \exp\left(-\frac{r^2}{w_0^2}\right) W(\mathbf{r}_t;k_t), \tag{1}$$

where $\mathbf{r}_t=(x,y)=(r,\phi)$ denotes the transverse coordinates, $W(\mathbf{r}_t;k_t)$ is the transverse pattern of the ideal nondiffracting beam given by $W(\mathbf{r}_t;k_t)\exp(ik_z z)$, and $w_0$ is the waist size of a Gaussian envelope. The transverse $k_t$ and longitudinal $k_z$ components of the wave vector $\mathbf{k}$ satisfy the relation $k^2=k_t^2+k_z^2$. The transverse distribution $W(\mathbf{r}_t;k_t)$ of the ideal nondiffracting beam fulfills the two-dimensional Helmholtz equation

$$\left(\frac{\partial^2}{\partial x^2}+\frac{\partial^2}{\partial y^2}+k_t^2\right)W(\mathbf{r}_t;k_t)=0, \tag{2}$$

and can be expressed as a superposition of plane waves whose transverse wave numbers $k_t$ are restricted to a single value, namely

$$W(\mathbf{r}_t;k_t)=\int_{-\pi}^{\pi}A(\varphi)\exp[ik_t(x\cos\varphi+y\sin\varphi)]\mathrm{d}\varphi, \tag{3}$$

where $A(\varphi)$ is the angular variation of the spectrum of the ideal nondiffracting beam.

By expanding the nondiffracting beam $W(\mathbf{r}_t;k_t)$ in terms of plane waves, we demonstrate in Ref. 10 that the propagated field $U(\mathbf{r})$ can be determined in terms of its boundary condition $U_0(\mathbf{r}_t)$ at $z=0$ written in Eq. (1). We obtain

$$U(\mathbf{r})=\exp\left(-i\frac{k_t^2}{2k}\frac{z}{\mu}\right)\mathrm{GB}(\mathbf{r})W\left(\frac{x}{\mu},\frac{y}{\mu};k_t\right), \tag{4}$$

where $\mathrm{GB}(\mathbf{r})$ is the fundamental Gaussian beam

$$\mathrm{GB}(\mathbf{r})=\frac{\exp(ikz)}{\mu}\exp\left(-\frac{r^2}{\mu w_0^2}\right), \tag{5}$$

and

$$\mu=\mu(z)=1+iz/z_R, \tag{6}$$

with $z_R=kw_0^2/2$ being the usual Rayleigh range of a Gaussian beam. Equation (4) is a solution of the paraxial wave equation subject to the boundary condition $U(z=0)=U_0(\mathbf{r}_t)$.

The angular spectrum of a HzG beam across a plane parallel to the $(x,y)$ plane at a distance $z$ from the origin is given by the two-dimensional Fourier transform

$$\bar{U}(u,v;z)=\frac{1}{2\pi}\int\int U(x,y,z)\exp(-ixu-iyv)\,\mathrm{d}x\,\mathrm{d}y, \tag{7}$$

where $(u,v)$ are the Cartesian coordinates in frequency space, and the double integral is carried out over the whole plane $(x,y)$. By substituting Eq. (4) into Eq. (7) we show in Ref. 10 that the spectrum of the HzG beams is given by

$$\bar{U}(u,v;z)=D(z)\exp\left(-\frac{w_0^2\mu}{4}\rho^2\right)W\left(\frac{w_0^2}{2i}u,\frac{w_0^2}{2i}v;k_t\right), \tag{8}$$

where $\rho=(u^2+v^2)^{1/2}$ is the transverse radius in the frequency space, and $D(z)=(w_0^2/2)\exp(ikz-k_t^2w_0^2/4)$ is a complex amplitude factor that depends on $z$ only.

Equations (4) and (8) constitute the general expression of the HzG beam and its spectrum, respectively. The propagation properties of the HzG beams are discussed in detail from a theoretical point of view in Ref. 10.

## 3 Generation of the Four Fundamental Families of Helmholtz-Gauss Beams

In order to generate and study the propagation of HzG beams of different classes, we have used the experimental setup depicted in Fig. 1. A Fourier computer-generated hologram (CGH) was illuminated with a plane wave from a spatially-filtered HeNe 15 mW laser at $\lambda=632.8$ nm. The resulting field distribution immediately after the CGH was then focused by a converging Fourier lens $L_1$ with focal distance $f_1$ and the order of diffraction +1 was filtered with an iris diaphragm (not shown) at the Fourier plane.

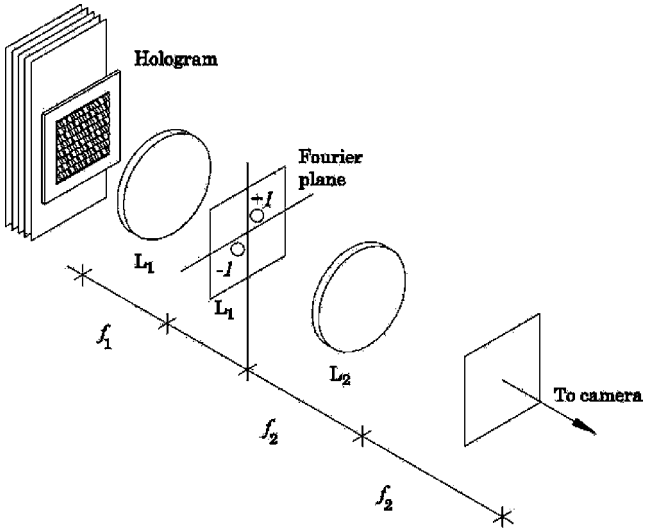


**Fig. 1** Experimental setup for the reconstruction of the holographic HzG beams. The spectrum is filtered at the Fourier plane by a circular diaphragm (not shown).

Once the desired spectrum was obtained, the HzG beam was reconstructed using a variation of Durnin's original setup.[2,3] In Durnin's experiment, an anular thin slit was backlit by a plane wave, which resulted in a zeroth-order Bessel beam upon focusing. In our case, the field at the Fourier plane acts as the annular light source, which in our experiment is also properly modulated in amplitude and phase according to the angular spectrum of the desired field. Reconstruction of the HzG beam is achieved with a second converging lens $L_2$ with focal distance $f_2$ in front of the diaphragm.

The CGH was computed using a numerical routine which calculates the complex field that results from interfering the linearly polarized HzG transverse field and an inclined plane wave with the same polarization. The phase of the resulting interference field distribution was then converted to grayscale values and subsequently photoreduced onto black and white photographic film. A phase hologram resulted after the film was developed and subsequently bleached.

The inclination of the reference plane wave determines the separation of the diffraction orders in the Fourier plane. Since the spatial phase of the reference wave at the hologram plane essentially resembles a sawtooth function, the CGH acts as a diffraction grating that produces the desired intensity profile at the first diffraction order, spatially separated from the undiffracted light of the illumination source. An appropriate choice of the inclination sets the spectrum far away from the optical axis for the purpose of avoiding the high intensity of the zeroth diffraction order and the higher diffraction orders containing harmonic noise.

In the following subsections, we investigate the propa-

gation characteristics of an example of HzG beams corresponding to each fundamental family of ideal nondiffracting beams. Namely plane waves in Cartesian coordinates, Bessel beams in circular cylindrical coordinates,[2,3] Mathieu beams in elliptic cylindrical coordinates,[4–6] and parabolic beams in parabolic cylindrical coordinates.[7]

### 3.1 *Generation of Cosine-Gauss Beams*

The cosine field

$$W(\mathbf{r}_t;k_t)=\cos(k_t y) \tag{9}$$

resulting from the superposition of two ideal plane waves $\exp(ik_t y)/2+\exp(-ik_t y)/2$ is one of the simplest examples of a nondiffracting beam in Cartesian coordinates. Its angular spectrum is $A(\varphi)=\delta(\varphi-\pi/2)+\delta(\varphi+\pi/2)$, where $\delta(\cdot)$ is the Dirac delta function.

Taking Eq. (9) as the functional form of $W$ in Eq. (4), the resulting field is the cosine-Gauss (CG) beam

$$\mathrm{CG}(\mathbf{r})=\exp\left(-i\frac{k_t^2}{2k}\frac{z}{\mu}\right)\mathrm{GB}(\mathbf{r})\cos\left(\frac{k_t y}{\mu}\right). \tag{10}$$

To verify the propagation features of the HzG beams, we have recorded the transverse intensity profiles along the propagation coordinate $z$ at different distances from the waist. As predicted in Ref. 10, the conical superposition of the Gaussian components of the beam will be significant along a geometrical distance

$$z_{\max}=w_0 k/k_t \tag{11}$$

measured from the waist plane. For the CG beam we have used a Gaussian waist $w_0=0.9$ mm and the transverse component of the spatial frequency $k_t=2.2\times10^4$ m$^{-1}$ for computing the hologram, so that $z_{\max}=40.2$ cm.

Transverse intensity profiles of CG beams are shown in Fig. 2(a), 2(b), and 2(c) for $z/z_{\max}=0$, 0.8, and 1.6, respectively. The field is characterized by horizontal fringes whose separation is about $\pi/k_t\sim0.14$ mm. Note that the field spreads towards the outermost region of the transverse plane, as expected from a Gaussian beam. However, the horizontal fringes in the region surrounding the $z$ axis remain essentially diffractionless. Also depicted in Fig. 2(d) is the intensity upon propagation in the plane $(y,z)$. The three-dimensional beam distribution was obtained by recording the transverse field at 30 transverse planes evenly spaced through the range $0\leqslant z\leqslant 1.6z_{\max}$. From Fig. 2, it is clear that the CG beam behaves like a nondiffracting cosine field within the range $|z|\leqslant z_{\max}$. At the plane $z=0$ the field reduces to $\exp(-r^2/w_0^2)\cos(k_t y)$.

The spectrum of the CG beam is determined directly from Eq. (8) and (9), after using the identity $\cos(\pm ix)=\cosh(x)$ we obtain

$$\overline{CG}(u,v;z)=D(z)\exp\left(-\frac{\mu w_0^2}{4}\rho^2\right)\cosh[2\gamma^2(v/k_t)]. \tag{12}$$

In Fig. 2(e) and 2(f) we show the pattern recorded at the Fourier plane (see Fig. 1). The pattern corresponds to the spectrum of the CG beam and is plotted as a function of the normalized spatial frequencies. As expected, the angular

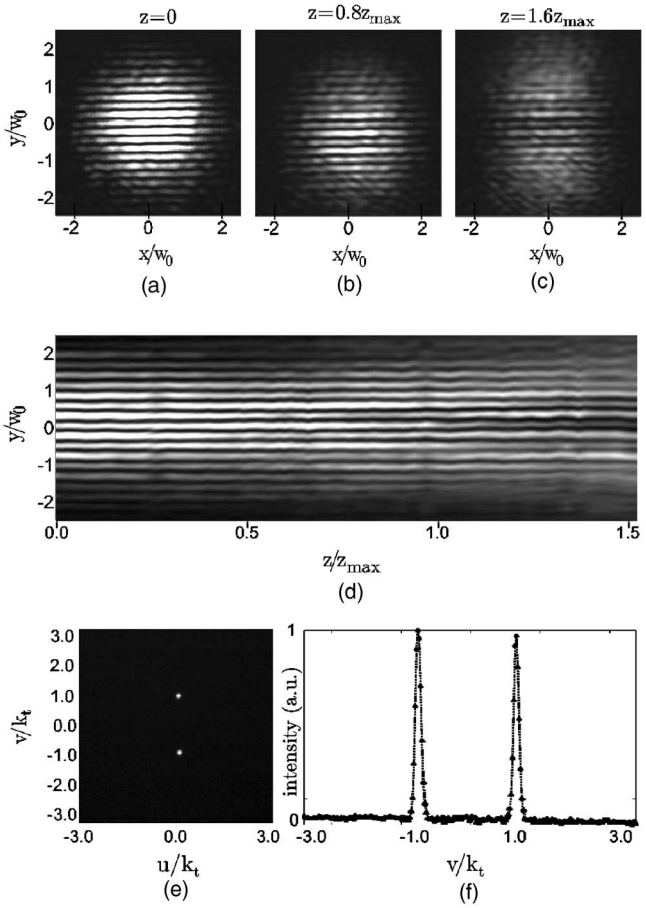


**Fig. 2** (a)–(c) Experimental transverse intensity distribution of a cosine-Gauss beam at different $z$ planes; (d) propagation of the intensity along the $(y,z)$ plane; (e) intensity distribution of the power spectrum in the Fourier plane; (f) transverse cut of the intensity distribution $(u=0)$ at the Fourier plane. The dashed line is the theoretical spectrum, also plotted for comparison.

spectrum of the CG beam is represented by two Gaussian-like spots placed at $(u,v)=(0,\pm k_t)$ and whose individual half-width is about $2/w_0$. Figure 2(f) shows an intensity plot along the $v$ axis in the Fourier plane at $u=0$. The theoretical intensity distribution is plotted for comparison.

### 3.2 *Generation of Bessel-Gauss Beams*

BG beams have been studied theoretically[8,10,17,18] and experimentally[19] elsewhere; in this subsection we briefly report their holographic generation for completeness.

The transverse field of the $m$'th-order Bessel beam reads as

$$W(\mathbf{r}_t;k_t)=J_m(k_t r)\exp(im\phi), \tag{13}$$

where $J_m(\cdot)$ is the $m$'th-order Bessel function. The angular spectrum of the Bessel beams is located on a single ring of radius $\rho=k_t$ in the frequency space and its angular dependence is $A(\varphi)\propto\exp(im\varphi)$. From Eq. (4), the BG beams are given by

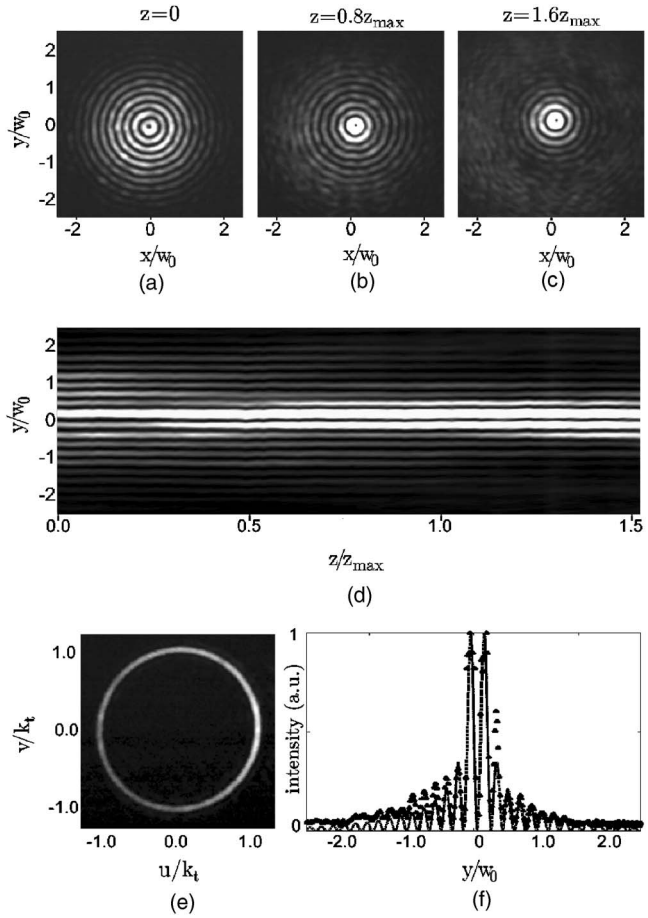


**Fig. 3** (a)–(c) Experimental transverse intensity distribution of a Bessel-Gauss beam at different $z$ planes; (d) propagation of the intensity along the $(y,z)$ plane; (e) intensity distribution of the power spectrum in the Fourier plane; (f) transverse cut of the intensity profile of the beam at the waist. The dashed line is the theoretical intensity distribution.

$$\mathrm{BG}_m(\mathbf{r}) = \exp\left(-i\frac{k_t^2}{2k}\frac{z}{\mu}\right)\mathrm{GB}(\mathbf{r})J_m\left(\frac{k_t r}{\mu}\right)\exp(im\phi). \tag{14}$$

We generated a first-order BG beam with a 0.9-mm waist and $k_t = 2.6\times10^4$ m$^{-1}$ for a distance $z_{\max}=31.9$ cm. Transverse intensity profiles are shown in Fig. 2(a), 2(b), and 2(c) for $z/z_{\max}=0$, 0.8, and 1.6, respectively. The loci of radial minima remains constant as the beam propagates, however the outermost nodal lines become undefined as the beam propagates. It can also be seen from the intensity along the $(y,z)$ plane shown in Fig. 3(d) that the central region of the beam remains invariant upon propagation regarding its intensity whereas the intensity becomes dimmer away from the axis.

The angular spectrum of the BG beams is determined directly from Eq. (8) and (13), after using the identity $J_m(-ix)=(-i)^m I_m(x)$ we obtain

$$\overline{BG}_m(u,v;z) = (-i)^m D(z)\exp\left(-\frac{\mu w_0^2}{4}\rho^2\right) \times I_m(2\gamma^2\rho/k_t)\exp(im\phi), \tag{15}$$

where $I_m(\cdot)$ is the $m$'th order modified Bessel function of the first kind. For the values used in the experiment, the spectrum is represented by a uniform annular ring whose mean radius is $k_t$ and whose width is defined by only the parameter $w_0$ of the Gaussian factor. In Fig. 3(e) we show the intensity of the measured spectrum at the Fourier plane of Fig. 1. It is expected that the intensity of the ring will be independent of the azimuthal coordinate; however, the ring amplitude is skewed towards the right due to crosstalk from the zeroth diffraction order. A similar situation occurs at the $-1$ diffraction order, where the skew is towards the left. The intensity cut of Fig. 3(f) correlates well with the theoretical BG profile (dashed line). The location of minima corresponds with the theoretical BG intensity distribution, except the threshold noise of the camera becomes evident in the outermost lobes of the beam.

### 3.3 *Generation of Mathieu-Gauss Beams*

The existence of the Mathieu beams was theoretically and experimentally demonstrated in recent papers.[4–6] The exact analytical expression for the Mathieu-Gauss beams of any order was reported and their properties were discussed in Ref. 10. To our knowledge, the experimental verification of MG beams has not been reported before.

#### 3.3.1 *Stationary Mathieu-Gauss beams*

The closed-form expression of the $m$'th-order even and odd MG beams is given by

$$\mathrm{MG}_m^e(\mathbf{r},q) = \exp\left(-i\frac{k_t^2}{2k}\frac{z}{\mu}\right)\mathrm{GB}(\mathbf{r})\mathrm{Je}_m(\bar{\xi},q)\mathrm{ce}_m(\bar{\eta},q), \tag{16}$$

$$\mathrm{MG}_m^o(\mathbf{r},q) = \exp\left(-i\frac{k_t^2}{2k}\frac{z}{\mu}\right)\mathrm{GB}(\mathbf{r})\mathrm{Jo}_m(\bar{\xi},q)\mathrm{se}_m(\bar{\eta},q), \tag{17}$$

where $\mathrm{Je}_m(\cdot)$ and $\mathrm{Jo}_m(\cdot)$ are the $m$'th order even and odd radial Mathieu functions, and $\mathrm{ce}_m(\cdot)$ and $\mathrm{se}_m(\cdot)$ are the $m$'th order even and odd angular Mathieu functions, respectively.[20] The parameter $q=f_0^2k_t^2/4$ carries information about the transverse spatial frequency $k_t$ and the ellipticity of the coordinate system through $f_0$. In a transverse $z$-plane the complex elliptic variables $(\bar{\xi},\bar{\eta})$ are determined by the following relations

$$x = f_0(1+iz/z_R)\cosh\bar{\xi}\cos\bar{\eta} \tag{18a}$$

$$y = f_0(1+iz/z_R)\sinh\bar{\xi}\sin\bar{\eta}, \tag{18b}$$

with $f_0$ being the semi-focal separation at the waist plane $z=0$. While the elliptic variables $(\bar{\xi},\bar{\eta})$ at the plane $z=0$ are real, outside this plane they become complex in order to satisfy the requirement that the Cartesian coordinates $(x,y)$ keep real in the entire space.

The transverse intensity distribution of a holographically generated second-order even MG beam with $q=16$ is shown in Figs. 4(a), 4(b), and 4(c) for $z/z_{\max}=0$, 0.8, and 1.6, respectively. Elliptic and hyperbolic nodal lines are well defined and symmetrical about the $x$ and $y$ axes. The propagation of the intensity profiles along the planes $(y,z)$ and $(x,z)$ are depicted in Fig. 4(d). These plots were ob-

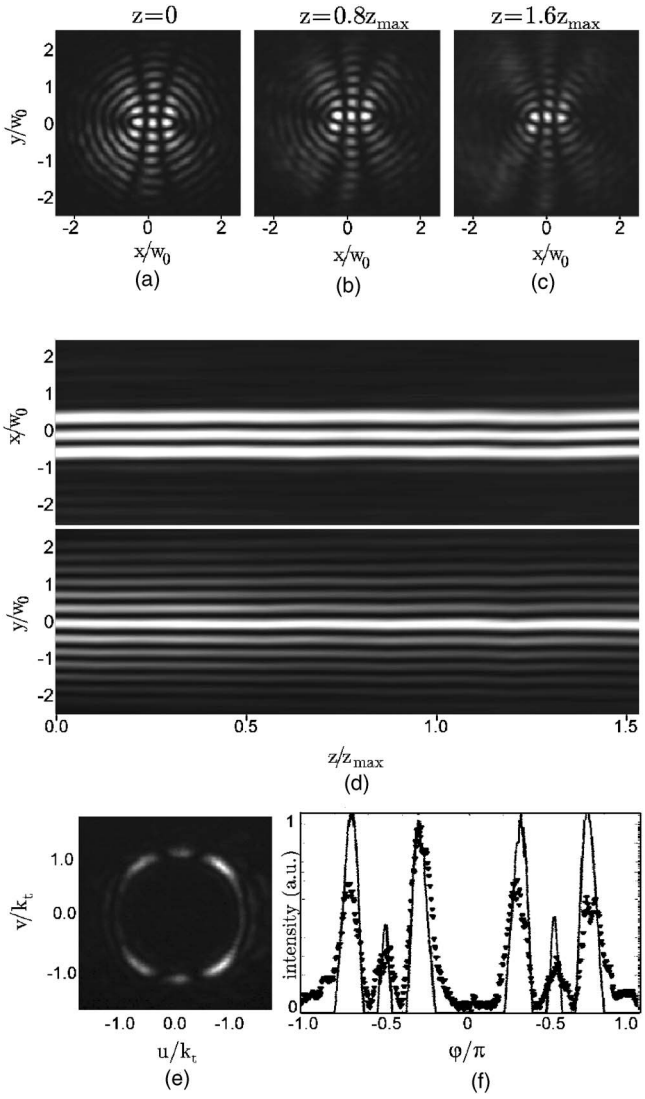


**Fig. 4** (a)–(c) Experimental transverse intensity distribution of a second-order even Mathieu-Gauss beam at different $z$ planes; (d) propagation of the intensity along the $(x,z)$ and the $(y,z)$ planes; (e) intensity distribution of the power spectrum in the Fourier plane; (f) angular cut ($\rho=k_t$) of the intensity distribution at the Fourier plane. The solid line is the theoretical intensity distribution, also plotted for comparison.

tained by recording the field at 30 transverse planes evenly spaced through the interval $[0,1.5z_{\max}]$. The MG beam behaves like a nondiffracting Mathieu beam within the measured range. Note that there exist only three maxima across the horizontal transverse coordinate $x$ and that each one of them remains well bounded and does not spread perceptibly up to a propagation distance of $1.5z_{\max}$.

The angular spectrum of the MG beams is given by

$$\overline{\mathrm{MG}}_m^e(u,v;z) = D(z)\exp\left(-\frac{\mu w_0^2}{4}\rho^2\right)\mathrm{Je}_m(\hat{\xi},q)\mathrm{ce}_m(\hat{\eta},q), \quad (19)$$

where the complex elliptic variables $(\hat{\xi},\hat{\eta})$ in the frequency space are determined by the following relations

$$u = \frac{2i}{w_0^2} f_0 \cosh\hat{\xi}\cos\hat{\eta}, \quad (20a)$$

$$v = \frac{2i}{w_0^2} f_0 \sinh\hat{\xi}\sin\hat{\eta}. \quad (20b)$$

In Fig. 4(e) and 4(f) we show the recording at the Fourier plane of the power spectrum of the $\mathrm{MG}_2^e$ beam as a function of the normalized coordinates $(u/k_t, v/k_t)$. As expected, the power spectrum is an azimuthally modulated annular ring with mean radius $\rho/k_t=1$ and angular dependence approximately given by the function $\mathrm{ce}_2^2(\varphi,q)$.

### 3.3.2 *Helical Mathieu-Gauss beams*

From the stationary mode solutions described by Eqs. (16) and (17) it is possible to construct Helical MG (HMG) beams of the form

$$\mathrm{HMG}_m^{\pm}(\mathbf{r},q) = A_m(q)\mathrm{MG}_m^e(\mathbf{r},q) \pm iB_m(q)\mathrm{MG}_m^o(\mathbf{r},q), \quad (21)$$

but whose phase rotates now elliptically around a strip defined by $(|x|\leq f,0,z)$. The coefficients $A_m(q)$ and $B_m(q)$ are normalization factors. Equation (21) is valid for $m>0$ because $\mathrm{MG}_m^o(\mathbf{r})$ is not defined for $m=0$. We show in Figs. 5(a), 5(b), and 5(c) the transverse experimental shapes of the helical beams $\mathrm{HMG}_7^{\pm}(\mathbf{r};q=16)$ at planes $z=0$, $0.8z_{\max}$, and $1.6z_{\max}$. The patterns consist of well defined elliptic confocal rings with a dark elliptic spot on axis. One could consider that the "stretching" of the beam's transverse intensity results in the unfolding of the vortex of charge $m$ at the center of a Bessel beam into the $m$ optical vortices of charge +1 that are located at the interfocal line of HMG beams. The HMG is characterized by an elliptic-helical phase that rotates about this line as the beam propagates. Intensity evolution along the $(x,z)$ and $(y,z)$ planes is each qualitatively similar to that of BG beams with different orders as shown in Fig. 5(d). In the limit $q\to 0$, they become identical and reduce to the case of the BG beam. Note that due to the elliptical-helical rotation of the phase, the orbital angular momentum density (OAM) of an HMG beam will vary azimuthally across the elliptic nodes of the beam, in contrast to the case of Bessel beams, where the azimuthal symmetry yields constant OAM density for a fixed radial coordinate.

The modulated circular ring in Fig. 5(e) is the intensity distribution at the Fourier plane. Crosstalk from the zeroth diffraction order is also present, resulting in a higher intensity towards the right side of the annuals. A plot of the beam intensity along the $x$ axis at the waist is shown in Fig. 5(f). The experimental data for the first radial maxima is significantly below the expected value due to the limited dynamic range of the camera used.

## 3.4 *Generation of Parabolic-Gauss Beams*

In a recent paper Bandrés et al.[7] demonstrated theoretically the existence of parabolic beams that constitute the fourth family of fundamental nondiffracting beams. Exact analytical expression for the parabolic-Gauss (PG) beams of any

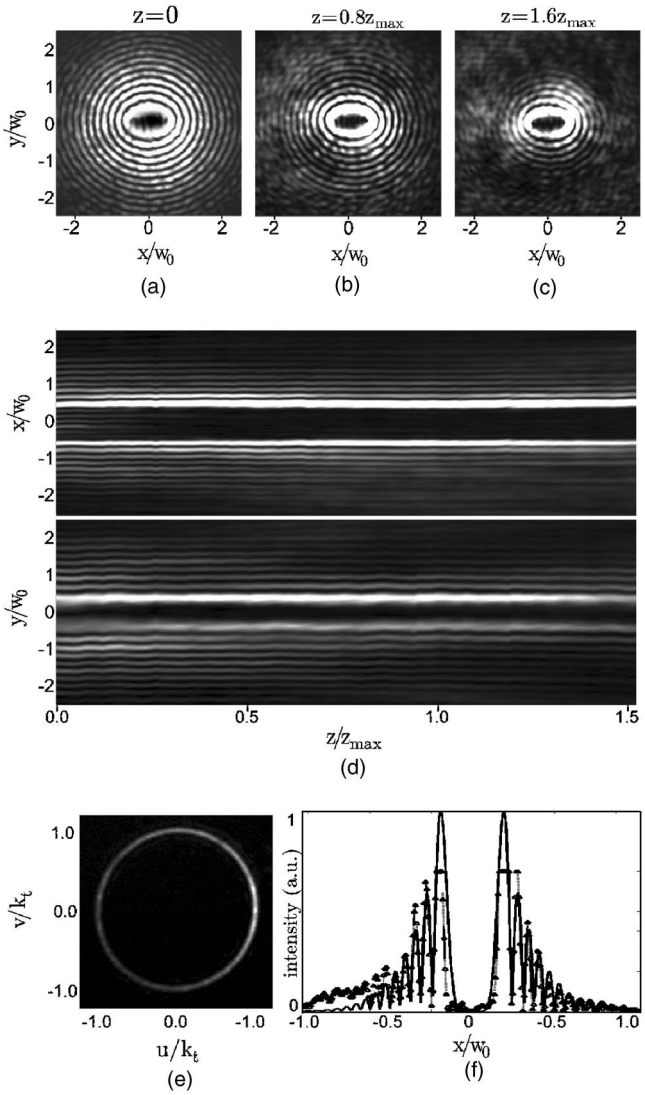


**Fig. 5** (a)–(c) Experimental transverse intensity distribution of a seventh order Helical Mathieu-Gauss beam at different $z$ planes; (d) propagation of the intensity along the $(x,z)$ and the $(y,z)$ planes; (e) intensity distribution of the power spectrum in the Fourier plane; (f) transverse cut at $y=0$ of the intensity profile of the beam at the waist. The dashed line is the theoretical intensity distribution.

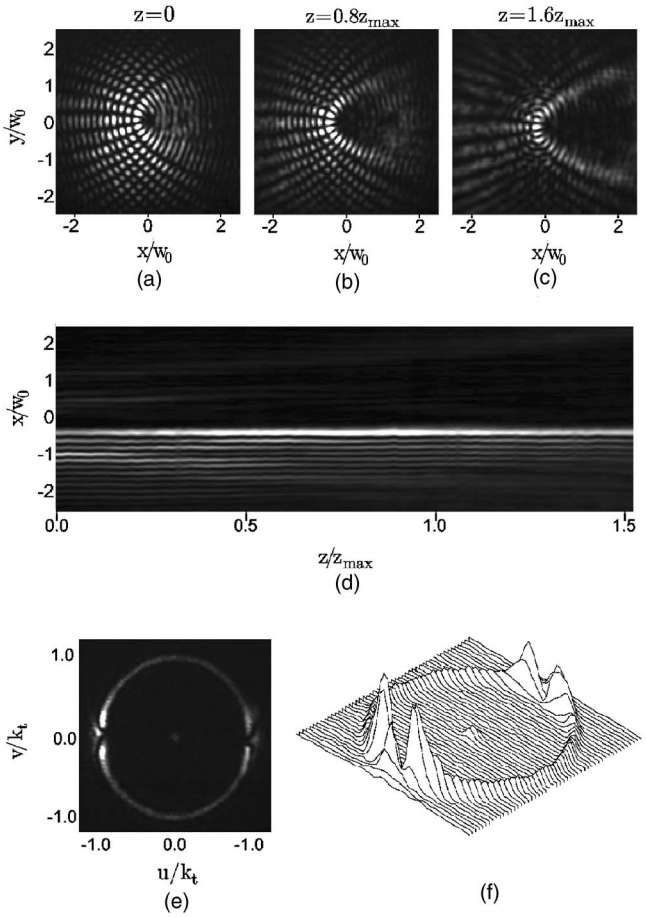


**Fig. 6** (a)–(c) Experimental transverse intensity distribution of an even Parabolic-Gauss beam of order $a=3$ at different $z$ planes; (d) propagation of the intensity along the $(x,z)$ plane; (e) distribution of the power spectrum in the Fourier plane; (f) surface contour plot of the power spectrum. Note the high peaks about the $v=0$ spatial frequency.

order was derived and their properties were discussed in Ref. 10. In this subsection we report for the first time the experimental generation of PG beams.

### 3.4.1 *Even parabolic-Gauss beams*

The parabolic cylindrical coordinates $(\xi,\eta)$ are defined by $x=(\eta^2-\xi^2)/2$, and $y=\xi\eta$, where the variables range in $\xi\in[0,\infty)$, $\eta\in(-\infty,\infty)$. In terms of the parabolic coordinates, the expressions for the even and odd PG beams are written as

$$\mathrm{PG}^o(\mathbf{r};a)=\exp\left(-i\frac{k_i^2}{2k}\frac{z}{\mu}\right)\mathrm{GB}(\mathbf{r})\frac{|\Gamma_1|^2}{\pi\sqrt{2}}\times \mathrm{P}_e(\sqrt{2k_t/\mu}\xi;a)\mathrm{P}_e(\sqrt{2k_t/\mu}\eta;-a), \tag{22a}$$

$$\mathrm{PG}^o(\mathbf{r};a)=\exp\left(-i\frac{k_t^2}{2k}\frac{z}{\mu}\right)\mathrm{GB}(\mathbf{r})\frac{|\Gamma_3|^2}{\pi\sqrt{2}}\times \mathrm{P}_o(\sqrt{2k_t/\mu}\xi;a)\mathrm{P}_o(\sqrt{2k_t/\mu}\eta;-a), \tag{22b}$$

where $\Gamma_1=\Gamma((1/4)+(1/2)ia)$, $\Gamma_3=\Gamma((3/4)+(1/2)ia)$, and the parameter $a$ represents the continuous order of the beam and can assume any real value in the range $(-\infty,\infty)$. The functions $\mathrm{P}_e(\cdot)$ and $\mathrm{P}_o(\cdot)$ are the even and solutions to the parabolic cylinder differential equation $[\mathrm{d}^2/\mathrm{d}x^2+(x^2/4-a)]\mathrm{P}(x;a)=0$.

The experimental intensity profiles for an even PG beam of order $a=3$ are shown in Figs. 6(a), 6(b), and 6(c). The patterns are characterized by confocal parabolic nodal lines. Figure 5(d) shows the evolution of the beam in the plane $(x,z)$ along the propagation coordinate. The residual noise at $x>0$ is quickly attenuated so that it becomes imperceptible after $z>0.4z_{\max}$.

The angular spectrum of the PG beams reads as

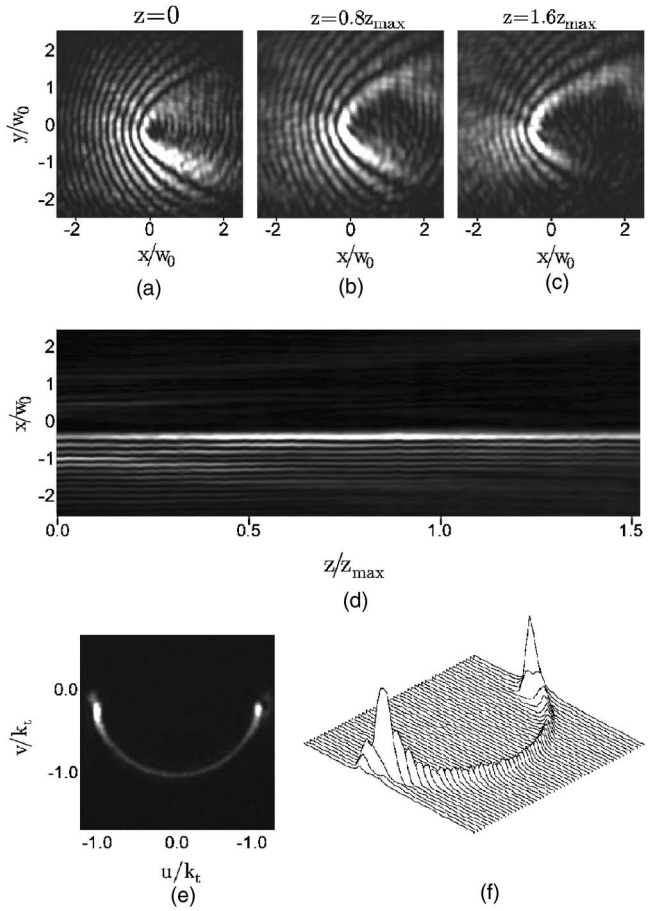


**Fig. 7** (a)–(c) Experimental transverse intensity distribution of a traveling parabolic-Gauss beam of order $a=3$ at different $z$ planes; (d) propagation of the intensity along the $(x,z)$ plane; (e) distribution of the power spectrum in the Fourier plane; (f) surface contour plot of the power spectrum. Note the semiannular profile with high intensity at $v=0$.

$$\overline{\mathrm{PG}}^{e}(u,v;z) = D(z)\exp\left(-\frac{\mu w_0^2}{4}\rho^2\right)\frac{|\Gamma_1|^2}{\pi\sqrt{2}} \times \mathrm{P}_e(\sqrt{-ik_t w_0^2}\,\tilde{\xi};a)\mathrm{P}_e(\sqrt{-ik_t w_0^2}\,\tilde{\eta};-a), \qquad (23)$$

where the parabolic coordinates $(\tilde{\xi},\tilde{\eta})$ in the frequency space are given by $u=(\tilde{\eta}^2-\tilde{\xi}^2)/2$, and $v=\tilde{\xi}\tilde{\eta}$. Figure 5(e) shows a photograph of the power spectrum. Note that high spatial horizontal frequency noise is present near $u=\pm k_t$ and also a dim constant offset can be seen at $u=0$. Noise near the boundaries of the spectrum is, however, spatially isolated from the shape of the spectrum. This can be more easily appreciated in Fig. 5(f), where the intensity profile is plotted as a surface contour.

### 3.4.2 *Traveling parabolic-Gauss beams*

From the stationary beam solutions described by Eqs. (22) it is possible to construct traveling parabolic-Gauss (TPG) beams of the form

$$\mathrm{TPG}^{\pm}(\mathbf{r};a) = \mathrm{PG}^{e}(\mathbf{r};a) \pm i\mathrm{PG}^{o}(\mathbf{r};a). \qquad (24)$$

We show in Figs. 7(a), 7(b), and 7(c) the transverse experimental shapes of the traveling beams $\mathrm{TPG}^{-}(\eta,\xi;a=3)$ at planes $z=0$, $0.8z_{\max}$, and $1.6z_{\max}$. Parabolic nodal lines and fringes along constant $\xi$ are clearly defined. The propagation sequence along the plane $(x,z)$ shown in Fig. 7(d) was obtained by recording the transverse field at 30 transverse planes evenly spaced through the range $0\leqslant z\leqslant 1.5z_{\max}$.

In the same way that the energy in the BG and HMG beams rotates around the beam axis and the interfocal line, respectively, we have verified that the energy in the TPG beams flows along the parabolic fringes as the beam propagates. Actually, this transverse energy flow is needed to guarantee that the far field of the TPG beams will tend to the semi-annular profile given by the angular spectrum. The power spectrum of the TPG beam shown in Figs. 7(e) and 7(f) was recorded at the Fourier plane shown in Fig. 1. Note that the noise found in the spectrum of the even PG beam was not present in the spectrum of the TPG beam.

## 4 Conclusions

We have experimentally generated and characterized HzG beams of all the four different classes: cosine-Gauss, Bessel-Gauss, Mathieu-Gauss, and parabolic-Gauss. Unlike ideal nondiffracting beams, HzG beams carry finite energy and can be experimentally generated to a very good approximation. The experimental results confirmed that HzG behave as nondiffracting beams within the range $|z|\leqslant z_{\max}$. Transverse energy flux has been observed in the case of high-order BG beams, HMG beams, and TPG beams. This behavior is due to the transverse phase distribution of the beams and portraits important consequences regarding the OAM density of these beams.

HzG beams are suitable for use in applications where nondiffracting beams are indicated, with the added advantage that their funcional form is more accurately realizable in the laboratory and their energy content is well bounded by their Gaussian envelope. Additionally, the OAM content of HzG beams allow for the manipulation of and transfer of OAM to particles. This particular feature of HzG beams is of particular interest in microfluidics, where an HzG beam can be used to move particles in definite trajectories using one single beam.

### *Acknowledgments*

The authors wish to acknowledge financial support from Conacyt-México grant 42808, and from the Tecnológico de Monterrey Research Chair in Optics grant CAT-007.

### *References*

1. Z. Bouchal, "Nondiffracting optical beams: physical properties, experiments, and applications," *Czech. J. Phys., Sect. A* **53**, 537–578 (2003).
2. J. Durnin, "Exact solutions for nondiffracting beams. I. The scalar theory," *J. Opt. Soc. Am. A* **4**(4), 651–654 (1987).
3. J. Durnin, J. J. Micely, Jr., and J. H. Eberly, "Diffraction-Free Beams," *Phys. Rev. Lett.* **58**(15), 1499–1501 (1987).
4. J. C. Gutiérrez-Vega, M. D. Iturbe-Castillo, and S. Chávez-Cerda, "Alternative formulation for invariant optical fields: Mathieu beams," *Opt. Lett.* **25**(20), 1493–1495 (2000).
5. J. C. Gutiérrez-Vega, M. D. Iturbe-Castillo, G. A. Ramírez, E. Tepichín, R. M. Rodríguez-Dagnino, S. Chávez-Cerda, and G. H. C. New, "Experimental demonstration of optical Mathieu beams," *Opt. Commun.* **195**(1), 35–40 (2001).
6. S. Chávez-Cerda, M. J. Padgett, I. Allison, G. H. C. New, J. C. Gutiérrez-Vega, A. T. O'Neil, I. MacVicar, and J. Courtial, "Holographic generation and orbital angular momentum of high-order Mathieu beams," *J. Opt. B: Quantum Semiclassical Opt.* **4**, S52–S57

(2002).
7. M. A. Bandrés, J. C. Gutiérrez-Vega, and S. Chávez-Cerda, "Parabolic nondiffracting wave-fields," *Opt. Lett.* **29**(1), 44–46 (2004).
8. F. Gori, G. Guattari, and C. Padovani, "Bessel-Gauss beams," *Opt. Commun.* **64**(6), 491–495 (1987).
9. A. P. Kiselev, "New structures in paraxial Gaussian beams," *Opt. Spectrosc.* **96**(4), 479–481 (2004).
10. J. C. Gutiérrez-Vega and M. A. Bandrés, "Helmholtz-Gauss beams," *J. Opt. Soc. Am. A* **22**(2), 289–298 (2005).
11. C. López-Mariscal, M. A. Bandrés, S. Chávez-Cerda, and J. C. Gutiérrez-Vega, "Observation of parabolic nondiffracting wave fields," *Opt. Express* **13**(7), 2364–2369 (2005).
12. C. Lopez-Mariscal, M. A. Bandrés, and J. C. Gutierrez-Vega, "Characterization of Helmholtz-Gauss beams," in *Laser Beam Shaping VI*, Fred M. Dickey and David L. Shealy, Eds., *Proc. SPIE* **5876**, 58760B (2005).
13. K. P. Volke-Sepúlveda, V. Garcés-Chávez, S. Chávez-Cerda, J. Arlt, and K. Dholakia, "Orbital angular momentum of a high-order Bessel light beam," *J. Opt. B: Quantum Semiclassical Opt.* **4**, S82–S89 (2002).
14. M. Erdélyi, Z. L. Horváth, G. Szabó, S. Bor, F. K. Tittel, J. R. Cavallaro, and M. C. Smayling, "Generation of diffraction-free beams for applications in optical microlithography," *J. Vac. Sci. Technol. B* **15**, 287–298 (1997).
15. Y. F. Lu and J. F. Greenleaf, "A study of two-dimensional array transducers for limited diffraction beams," *IEEE Trans. Ultrason. Ferroelectr. Freq. Control* **41**, 724–739 (1994).
16. Y. F. Lu and S. He, "Optical X wave communications," *Opt. Commun.* **161**, 187–192 (1999).
17. J. C. Gutiérrez-Vega, R. Rodríguez-Masegosa, and S. Chávez-Cerda, "Axicon-based Bessel-Gauss resonator with spherical output mirror: geometrical and wave optics analysis," *J. Opt. Soc. Am. A* **20**(11), 2113–2122 (2003).
18. Y. Li, H. Lee, and E. Wolf, "New generalized Bessel-Gaussian beams," *J. Opt. Soc. Am. A* **21**(4), 640–646 (2004).
19. A. Hakola, S. C. Buchter, T. Kajava, H. Elfström, J. Simonen, P. Pääkkönen, and J. Turunen, "Bessel-Gauss output beam from a diode-pumped Nd:YAG laser," *Opt. Commun.* **238**(4), 335–340 (2004).
20. J. C. Gutiérrez-Vega, R. M. Rodríguez-Dagnino, M. A. Meneses-Nava, and S. Chávez-Cerda, "Mathieu functions, a visual approach," *Am. J. Phys.* **71**(3), 233–242 (2003).

**Carlos López-Mariscal** received his BS and MSc degrees from Tecnológico de Monterrey in Monterrey, México, in 1998 and 2003, respectively. He is currently a PhD student with the Photonics and Mathematical Optics Group at Tecnológico de Monterrey. In 2005 he received the Newport Spectra-Physics Research Excellence Award and in 2006 he was awarded a SPIE scholarship.

**Miguel A. Bandrés** received his BS degree from Tecnológico de Monterrey in Monterrey, México, in 2002. He was with the Photonics and Mathematical Optics Group at Tecnológico de Monterrey during 2003–2004 and currently he is a graduate student at California Institute of Technology. In 2005 and 2006 he has been awarded the SPIE Student Scholarship.

**Julio C. Gutiérrez-Vega** received the BS degree in physics (1991) and MS degree in electric engineering (1995) from Tecnológico de Monterrey. In 2000, he received his PhD degree in optics from INAOE in Puebla, México. He currently heads the Optics Center and the Photonics and Mathematical Optics Group at Tecnológico de Monterrey. Dr. Gutiérrez-Vega is a member of SPIE, OSA, and IEEE.